International Journal of Plasticity 65 (2015) 33–42

Contents lists available at ScienceDirect

International Journal of Plasticity

journal homepage: www.elsevier.com/locate/ijplas

Concurrent atomistic–continuum simulations of dislocation–void interactions in fcc crystals

Liming Xiong [a,*], Shuozhi Xu [c], David L. McDowell [b,c], Youping Chen [d]

[a] Department of Aerospace Engineering, Iowa State University, Ames, IA 50011, USA
[b] School of Materials Science and Engineering, Georgia Institute of Technology, Atlanta, GA 30332, USA
[c] Woodruff School of Mechanical Engineering, Georgia Institute of Technology, Atlanta, GA 30332, USA
[d] Department of Mechanical and Aerospace Engineering, University of Florida, Gainesville, FL 32611,USA

ARTICLE INFO

Article history:
Received 28 October 2013
Received in final revised form 4 August 2014
Available online 20 August 2014

Keywords:
A. Dislocations
A. Strengthening mechanisms
B. Metallic material
C. Finite elements
C. Numerical algorithms

ABSTRACT

Dislocation interactions with distributed condensed vacancy clusters in fcc metals were simulated via a concurrent atomistic–continuum method. Due to void strengthening, the dislocation lines are found to bow as a result of pinning on the original glide plane and undergo depinning through drawing out screw dipoles and forming prismatic loops on the secondary slip plane. We discovered an inertia-induced transition between Hirsch looping and void shearing mechanisms as the void spacing ranges from the scale of nm to hundreds of nm. Contrary to prior understanding, simulations suggest that large voids (~5 nm in diameter) can behave as weak barriers to dislocation motions under high strain-rate dynamic conditions.

1. Introduction

Materials subjected to irradiation exhibit elevated yield strength and suffer from intrinsic softening and reduced ductility by virtue of localization of dislocation plasticity. Irradiation-induced defects act as obstacles to dislocation migration. Typical radiation-induced defects in fcc lattices include voids (Averback et al., 1977; Kluth et al., 2005; Kondo et al., 2008, Crocombette and Proville, 2011) and helium bubbles (Donnelly et al., 1983; Henriksson et al., 2005; Demkowicz et al., 2010; David et al., 2011), particularly for fusion applications (Zinkle, 2005). Transmission electron microscopy (TEM) studies indicate that these defects act as obstacles to dislocations and, when bypassed, lead to localization of deformation in regions where defect densities are reduced via dislocation interaction (Shilo and Zolotoabko, 2003, 2007; Shingo et al., 2007; Wu et al., 2007). Unfortunately, in situ observations of dislocation–obstacle interactions are quite limited owing to elaborate sample preparation, and restricted spatial and temporal ranges of TEM.

Static analysis of void strengthening suggests that voids with diameter of ~2 nm or larger generally act as 'strong obstacles', whereas voids with diameter less than ~2 nm act as 'weak obstacles', respectively (Hull and Bacon, 2001). It was concluded that the stress required for dislocation depinning from these voids approaches the theoretical Orowan stress (Hull and Bacon, 2001; Hirth and Lothe, 1982; Shim et al., 2007). For predicting the in-service performance of metals in fusion energy facilities, however, understanding of the influence of dynamic deformation on void strengthening mechanisms is crucial and requires atomistic insight of unit processes of dislocation–void interactions. In the past ten years, molecular dynamics (MD) has been used extensively to investigate dislocation–obstacle interactions in irradiated metals (Wu et al., 2007; Shim et al., 2007; Harry and Bacon, 2002; Osetsky and Bacon, 2003; Bacon and Osetsky, 2005; Bacon et al., 2006;

* Corresponding author.

http://dx.doi.org/10.1016/j.ijplas.2014.08.002
0749-6419/

Terentyev et al., 2007; Cheng et al., 2010). Major limitations arise in using MD to simulate large systems, for example systems with dislocation line lengths on the order of microns and void spacing on the order of hundreds of nanometers. Continuum simulation tools such as dislocation dynamics (DD) (Amodeo and Ghoniem, 1990a, 1990b; Kubin and Canova, 1992; Van der Giessen and Needleman, 1995; Zbib et al., 1998; Bulatov et al., 1998; Cai and Bulatov, 2004) provide approximate description of dislocations at these larger scales, based on elastic theory of lattice dislocations. However, DD typically suffers from the approximate nature of prescribed short-range interaction rules between mobile dislocations and obstacles, lacks the ability to model dislocation dissociation, and requires approximations for dislocation cross slip and other important local mechanisms.

Pioneering MD simulations of vibrating dislocations were conducted but limited to 2D Frenkel–Kontorowa models (Weiner et al., 1976). Those models neglected phonon drag effects. Recently, Gumbsch and co-workers (Cheng et al., 2010, Bitzek and Gumbsch, 2004, 2005) investigated dislocation depinning through MD simulations considering dynamic/inertial effects. Their results suggest that dynamic inertial effects significantly lower the depinning stress. It was suggested that such inertial effects should not be ignored in computational models at higher scales. However, continuum models, such as DD, typically assume overdamped dislocation migration via a constitutive force–velocity relationship.

Due to the spatio-temporal complexity of dislocation dynamics, various multiscale modeling methods (McDowell, 2010) including sequential (Amodeo and Ghoniem, 1990a, 1990b; Kubin and Canova, 1992; Van der Giessen and Needleman, 1995; Zbib et al., 1998; Bulatov et al., 1998; Cai and Bulatov, 2004; Shehadeh et al., 2006; Hu et al., 2007) and concurrent (Tadmor et al., 1996; Zhou and McDowell, 2002; Fago et al., 2004; Shilkrot et al., 2002a, 2002b; Zamora et al., 2012) approaches have been developed to describe dislocation physics. In sequential, hierarchical multiscale modeling approaches, it is intended that the characteristics and understanding of dislocation–obstacle interactions obtained from MD are incorporated in higher length scale continuum DD or crystal plasticity simulations. These parameters include maximum obstacle force, critical cusp angle, and Peierls stress. Although particular long range dislocation–obstacle interactions can be represented within continuum treatments, it is difficult if not impossible to address complex short range interactions and processes (e.g., core interactions). Concurrent approaches such as the Quaiscontinuum method (QC) (Tadmor et al., 1996; Fago et al., 2004) or Coupled Atomistics Discrete Dislocation (CADD) (Shilkrot et al., 2002a, 2002bb; Zamora et al., 2012) seek to address the crucial question of how to reconcile a consistent treatment of dislocations that pass between atomic and continuum regions; heuristic numerical techniques and/or rules are invoked for passing dislocations across interfaces between atomistic and continuum domains or through coarse-grained continuum domains with adaptive mesh refinement. As a consequence of these specialized treatments, existing concurrent approaches are only suitable for 2D quasistatic simulations of dislocations. For 3D dynamic dislocation–obstacle interactions, the recently developed concurrent atomistic–continuum (CAC) method (Xiong et al., 2011, 2012a, 2012b) is suitable as a formal coarse-graining of MD and is pursued in this work.

2. Methodology

Fundamental to the CAC method is a unified formulation of atomistic and continuum representation of balance laws (Chen and Lee, 2005; Chen, 2006, 2009). The CAC formulation generalizes Kirkwood's statistical mechanical theory of transport processes (Kirkwood, 1946; Irving and Kirkwood, 1950) to facilitate a two-level structural description of materials. It describes the structure of a crystalline material in terms of continuously-distributed lattice cells, but with a group of discrete atoms situated in each lattice cell at sub-structural level. A complete field representation of balance laws of atomistic systems is then derived. Under elastic distortion, the new balance equations fully reproduce the phonon dispersion relations (Xiong et al., 2014b). Consequently, the formulation reflects all possible dynamics on length and time scales from the atomic to the macroscopic, and admits coarse-graining in the context of a finite element formulation in which large numbers of atoms are contained within each element, with defects (e.g., dislocations or cracks) propagating along discontinuous element interfaces. This avoids anomalous effects of atomistic–continuum interfaces that hamper domain decomposition methods such as CADD (Shilkrot et al., 2002a, 2002b; Zamora et al., 2012), as well as finite temperature extensions of adaptively remeshed or reconfigured QC methods (Kulkarni et al., 2008). In contrast to most existing multiscale or coarse-grained methods (Chen et al., 2011), the representation of the complete set of balance laws renders CAC applicable to dynamic and nonequilibrium processes involving mass, momentum, and/or energy transport (Xiong et al., 2014b), with the interatomic potential or force field being the only empirical input. This work employs the embedded atom method potential (Daw and Baskes, 1984) for Ni (Mishin et al., 1999, 2001). The numerical implementation code of CAC is parallelized and is run on $N = 72$ processors, scaling as $O(N)$. The present work considers balance of mass and momentum, without addressing the energy equation, in view of the focus on dynamic effects of dislocation–void interactions.

3. Computational set-up and results

3.1. Effects of void spacings on the dislocation pinning–depinning

Fig. 1 shows the computational configuration of CAC models in this study. Single crystal Ni specimens ($\sim 50 \times 200 \times 100\ \text{nm}^3$) contain over 20 million atoms. The V-notch and four spherical voids with diameters of $\sim$5 nm are initially introduced into the models. The distance between the V-notch tip and the centers of the voids is $\sim$40 nm. Here

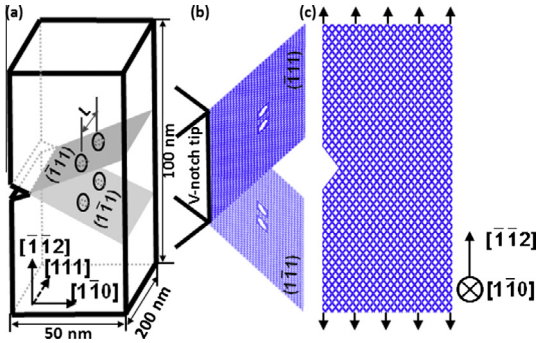

Fig. 1. Computational set-up: (a) V-notched specimens with spherical voids (diameter $D \approx 5$ nm) initially introduced to intersect active slip planes; (b) slices of the FE meshes (atomic resolution around the voids and coarse resolution away from the voids) on the slip planes; (c) frontal view of the CAC model (~100,000 elements representing ~20,500,000 atoms) with tensile loading applied along the $[\bar{1}\,\bar{1}\,2]$ direction.

the V-notch is employed to induce a highly localized stress concentration to drive the dislocations into the specimen to explore inertial effects of interactions with voids. Two voids are centered on the $(\bar{1}\,1\,1)$ slip planes on which notch root dislocations are expected to nucleate and the other two are similarly introduced on the $(1\,\bar{1}\,1)$ planes Fig. 1a. The voids have center-to-center spacing, L, ranging from 15 nm to 155 nm to facilitate parametric study. The specimens are discretized into ~100,000 finite elements (FE), each with rhombohedral shape corresponding to the primitive cell of fcc crystals (Xiong et al., 2011). Elements with full atomic resolution (i.e., 1 atom/element) are employed around the periphery of the voids to investigate the details of atomic scale dynamics during dislocation–obstacle interactions. Coarse scale elements (216 primitive cells/element) are employed away from the voids to reduce computational cost. Slices of FE meshes cutting through the voids are shown in Fig. 1b. Displacement-controlled tensile loading with a constant velocity of 5 m/s is applied on the two ends of the specimen Fig. 1c, corresponding to a strain rate of $\sim 10^7$/s. Lateral surfaces are traction free. It should be noted that the image forces resulting from the interactions between the dislocations and the free surfaces may have an effect on the pinning–depinning dynamics. The effects of such image forces are minimized in our simulations by arranging for pinning–depinning to occur near the center of the computational cell with the sample thickness being around 300 nm. Such a computational set-up for such a thick specimen assures that the image forces nearly cancel (Zhou et al., 1998). The central difference method (Δt = 5 fs) is employed for time integration and standard Gauss quadrature is used for spatial integration. In this work we focus on the mechanical aspect of dislocation–void interactions and hence a homogeneous low temperature field as low as T = 0.2 K is assumed. The deformation of the FE mesh and arrangements of atoms are simultaneously output from CAC simulations. Atomic positions are mapped from the FE nodal positions through interpolation (Xiong et al., 2011, 2012a, 2012b). For a Ni specimen ($L \approx 15$ nm), Fig. 2a presents the time sequences of dislocations (blue atoms) and stacking faults (red atoms) displayed through rendering the atoms using the centrosymmetry parameter in AtomEye (Li, 2003). Fig. 2b shows the FE mesh and the local shear stress (σ_{23}) distributions on the $(\bar{1}\,1\,1)$ slip planes. With continued tensile loading, dislocations initiate from the notch-tip, migrate on the slip planes and eventually interact with the voids.

It is seen from Fig. 2 that the dislocation–void interaction process can be divided into three stages: (1) the dislocation line encounters the voids at t = 0.110 ns; (2) the dislocation line bypasses the void surfaces from t = 0.114 ns to t = 0.116 ns; (3) the dislocation line breaks away at t = 0.117 ns under a critical (peak) resolved shear stress. The dislocation line bows when it enters the voids at t = 0.110 ns. At t = 0.114 ns, the dislocation line is clearly bowing out between voids. The segments on either side of the voids begin to move into parallel alignment. At t = 0.115 ns, due to dynamic effects, the dislocation segment around void-1 has enough kinetic energy to compensate the attraction from this void, and depinning occurs via 'overshooting'. The inertial overshooting of dislocations leads to a cusp angle ($\varphi_c \approx 120°$) larger than that typical of a static bow-out (Bitzek and Gumbsch, 2004, 2005; Granato, 1971; Fusenig and Nembach, 1993). Here the depinning cusp angle is measured at the instant in time at which the dislocation line detaches from the void. Thereafter, the depinning of dislocation line from void-1 immediately slows down the rate of dislocation migration and results in a Hirsch depinning process (Hirsch et al., 1958) at void-2. At t = 0.116 ns, the initially straight dislocation line is pulled into screw orientation by self-interaction. A screw dislocation dipole is formed with the assistance of the mutual attraction of the two dislocation branches emerging from the void surfaces. Before the formation of the full dipole, a partial dislocation nucleates on the surface of void-2 at t = 0.117 ns. Thereafter an intrinsic prismatic loop is produced on the $(1\,\bar{1}\,1)$ plane. The diameter of the prismatic loop is nearly equivalent to the radius of void-2. The nucleation and the formation of the intrinsic dislocation loop enhances pinning of the next dislocation and generally inhibits depinning of dislocations on the primary system encountering the void. It is noted that the formation of intrinsic prismatic Hirsch loops has been observed in high strain rate experiments (Hirsch et al., 1958; Kiritani et al., 1999; Brown and Stobbs, 1971; Wusatowska-Sarnek et al., 1999). After t = 0.117 ns, the dislocation begins to detach from void-2 with a small cusp angle ($\varphi_c \approx 45°$). Eventually, the induced curvature of the dislocation line via interaction with void-2 becomes negligible when the dislocation line is about 10 lattice units away from the voids at t = 0.120 ns. Moreover, the prismatic loop on the $(1\,\bar{1}\,1)$ plane remains in plane as a sessile remnant of the interaction.

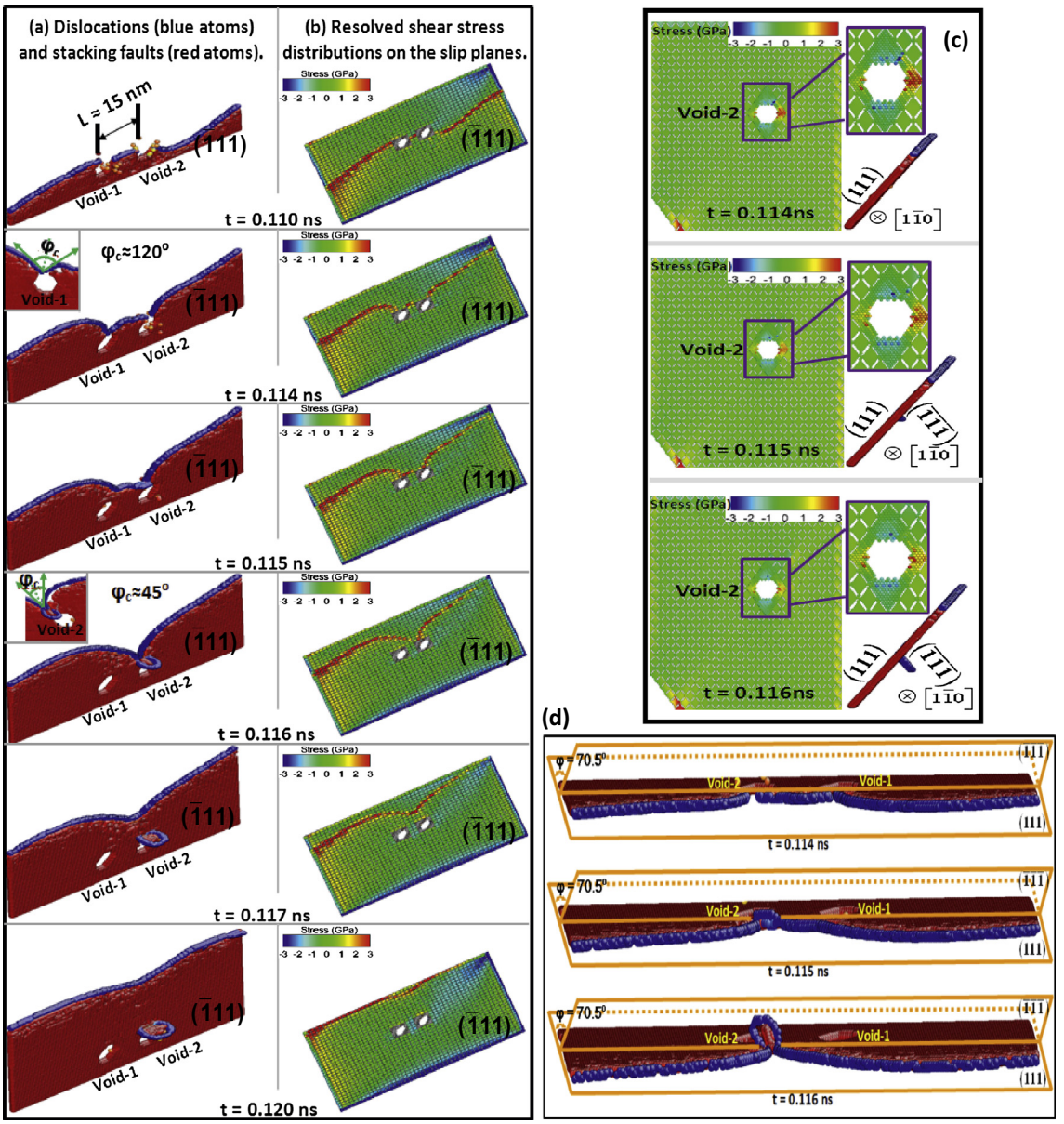

Fig. 2. Time sequence of snapshots of (a) dislocation and stacking fault structures projected on the (1 1 1) plane; (b) the shear stress distribution on the (1 1 1) plane; (c) the shear stress (σ_{23}) on the (1 $\bar{1}$ 0) plane; (d) dislocation and stacking fault structures on the ($\bar{1}$ 1 1) and (1 $\bar{1}$ 1) planes.

Two dislocations with Burgers vectors $\frac{1}{2}[1\,\bar{1}\,0]$ and $\frac{1}{2}[0\,1\,1]$ are emitted from the notch on the two respective inclined ($\bar{1}\,1\,1$) and ($1\,\bar{1}\,1$) glide planes. These dislocations have leading and trailing partial dislocations separated by a stacking fault. Due to the symmetry of the geometry and the boundary conditions applied on the computational models, we present only the results of the dislocation pinning–depinning from the voids in the upper part of the material body in Fig. 2, focusing on the initial encounter. With increase of tensile loading, more dislocations will be emitted from the V-notch tip, migrating toward the voids and eventually interacting. The atomic-scale mechanisms associated with the dislocation depinning from the deformed voids with successive encounters will be much more complex than what we have observed in Fig. 2 and is not to be investigated in the present work.

To clarify the underlying physics of the formation of prismatic dislocation loops on the secondary slip plane, the time sequence of [1 $\bar{1}$ 0] projections of mesh deformation and stress distribution around void-2 are shown in Fig. 2c, and the [$\bar{1}$ 1 1]/[1 $\bar{1}$ 1] projections of the dislocation and stacking fault structures are presented in Fig. 2d. Stress concentration at the void leads to the nucleation of secondary dislocations with a different Burgers vector from the void surface (note the partial dislocations emerging from the primary stacking fault at $t = 0.115$ ns). The asymmetry of the resolved shear stress

on sides of void-2 is clearly evident in Fig. 2c leads to nucleation and formation of the secondary loop on one side of the void. This differs, of course, from loops formed on the original glide plane during the bypass process, commonly termed as Orowan loops (Hull and Bacon, 2001; Hatano, 2006).

Fig. 3a–c compares the time sequences of dislocations, stacking faults, and the local resolved shear stress distributions for Ni for void spacings of $L \approx 20$ nm, $L \approx 30$ nm and $L \approx 60$ nm, respectively. It is seen that the dislocation lines in Fig. 3a–c are similar in shape. The critical cusp angles around all of the obstacles are $\varphi_c \approx 45°$. Comparing Figs. 2 and 3, we see that inertial effects are only observed in Ni for narrower obstacle spacing such as $L \approx 15$ nm, as shown in Fig. 2. As the void spacing is increased to $L \approx 20$ nm, 30 nm, and 60 nm, it is observed in Fig. 3 that the Hirsch looping mechanism activates. Obviously, enhanced depinning via dislocation inertia is no longer evident for 20 nm $\leqslant L \leqslant$ 60 nm. Therefore, we conclude that the phenomenon of the inertial overshooting is sensitive to the void spacing.

Fig. 4a and b presents a time sequence of dislocations, stacking fault structures, and the local shear stress distributions for Ni with void spacing $L \approx 155$ nm. At $t = 0.113$ ns, the dislocation line encounters the voids. In contrast to Fig. 3a–c, Fig. 4a shows that the depinning from void-1 excites internal vibrations of dislocation lines. The induced waves travel along the dislocation lines and then assist the dislocation depinning from void-2 (e.g., "whip" effect), where a large cusp angle ($\varphi_c \approx 110°$) is observed (see Fig. 4g).

According to the classification of Hull and Bacon (2001) or Hirth and Lothe (1982), voids act as strong obstacles when $\varphi_c < 100°$ (Fig. 4c) and as weak obstacles for $\varphi_c > 100°$ (Fig. 4d). In the present dynamic simulation, for voids with diameter of approximately 5 nm, comparing the cusp angles in Fig. 4e ($L \approx 15$ nm), Fig. 4f ($L \approx 30$ nm), and Fig. 4g ($L \approx 155$ nm), voids act as weak barriers in some cases ($\varphi_c \approx 110°$ around void-1 in Fig. 4e, $L \approx 15$ nm), and as strong barriers in other cases in connection with the Hirsch looping mechanism ($\varphi_c \approx 45°$ around both void-1 and void-2 in Fig. 4f, $L \approx 30$ nm).

To identify the origin of the transition of deformation mechanism, we have conducted an additional CAC simulation ($L \approx 155$ nm) with large viscous damping to reduce the dynamic response. As shown in Fig. 4h, as a result of the viscous damping, the dislocation depinning does not occur until $t = 0.180$ ns and the cusp angle around void-2 dramatically decreases from 110° (Fig. 4g) to 70° (Fig. 4h) at $L \approx 155$ nm. That is, when the dynamic effect has been alleviated, void-2 acts as a strong barrier, in contrast to the weak barriers observed in the earlier dynamic simulation (Hull and Bacon, 2001; Bacon et al., 2009). It is believed that the depinning angles will approach values predicted by the static line tension models with further increase of the viscous damping coefficient in the CAC simulations. However, according to our recent predictions

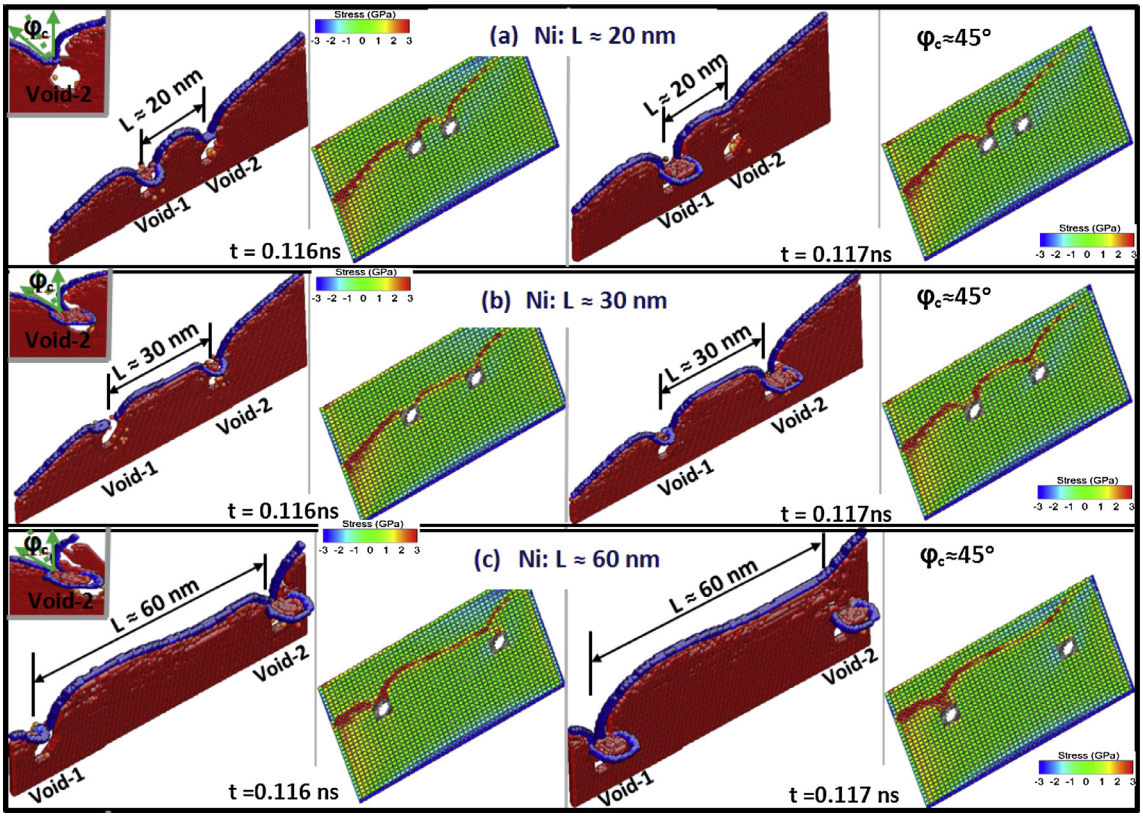

Fig. 3. Time sequences of snapshots of dislocations, stacking fault structures, and shear stress (σ_{23}) distributions on the (1 1 1) plane: (a) $L \approx 20$ nm; (b) $L \approx 30$ nm; (c) $L \approx 60$ nm.

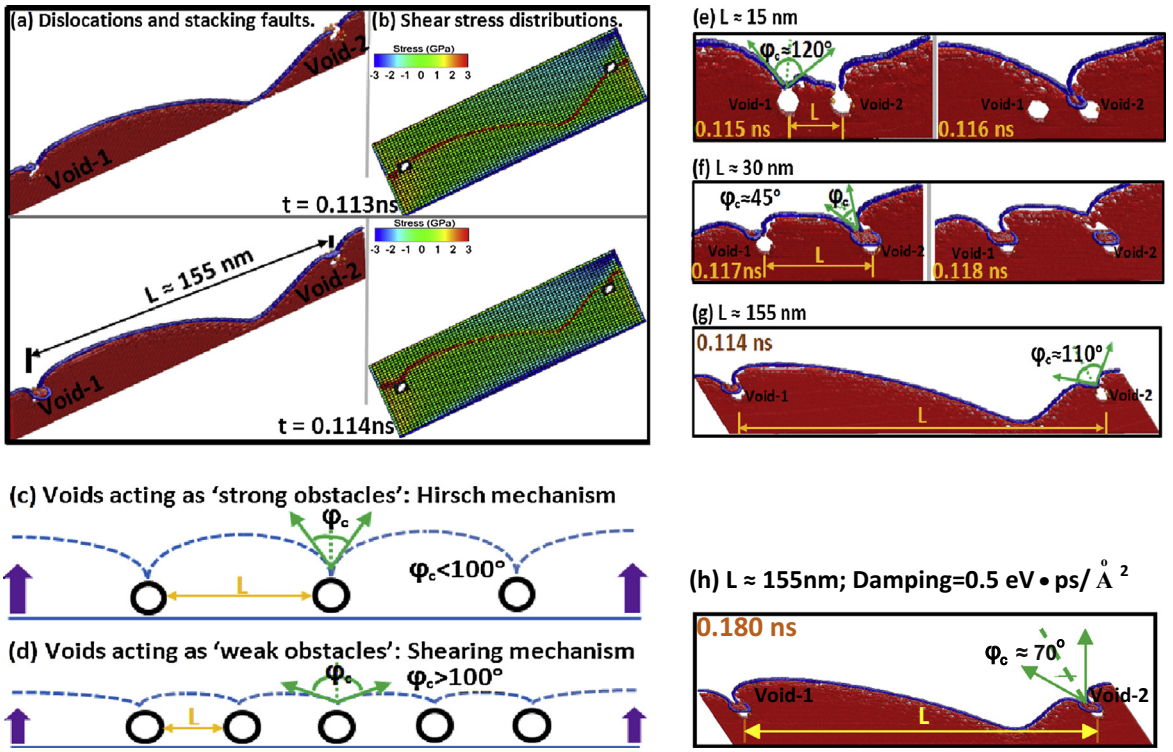

Fig. 4. Ni ($L \approx 155$ nm) under tension by CAC simulations: (a) time sequences of snapshots of dislocation and stacking fault structures on the (1 1 1) plane; (b) shear stress (σ_{23}) distributions during the dislocation–void interactions on the (1 1 1) plane; (c) voids acting as 'strong obstacles' via the Hirsch looping mechanism; (d) voids acting as 'weak obstacles' via shearing mechanisms; (e) void-1 ($\varphi_c \approx 120°$) acting as a 'weak obstacle', $L \approx 15$ nm; (f) voids-1,2 ($\varphi_c \approx 45°$) acting as 'strong obstacles', $L \approx 30$ nm; (g) void-2 ($\varphi_c \approx 110°$) acting as 'weak obstacles', $L \approx 155$ nm; (h) void-2 ($\varphi_c \approx 70°$) acting as a 'strong obstacle' in CAC simulations with a viscous damping, $L \approx 155$ nm.

(Xiong et al., 2014a), the viscous damping coefficient in our CAC simulation should not be an artificial parameter per se, but rather should be on the same order of phonon drag coefficients on dislocation motions in fcc crystals under high strain rate loading conditions.

3.2. Effects of notch tip stress field and strain-rates on the dislocation pinning–depinning

The stress state in the CAC models of nano-sized specimens is rendered complex by virtue of the presence of the V-notch. To assess the effects of the complex stress field associated with the V-notch tip on the dislocation pinning–depinning from the voids, we present initial stress distributions from the CAC computational models for distances between the V-notch tip and the center of the voids of 30 nm (Fig. 5a), 40 nm (Fig. 5b) and 50 nm (Fig. 5c), respectively. The dislocations (blue) and stacking faults (red) structures with the onset of the dislocation depinning from the voids in three different CAC models are also presented. It is seen that the largest depinning angles have been reproduced when the distance between the initially introduced voids and the V-notch tip is as close as $d = 30$ nm (Fig. 5a) comparing with those depinning angles from the computational models with $d = 40$ nm (Fig. 5b) and $d = 50$ nm (Fig. 5c). Therefore, it is believed that stronger inertial effects will be induced to drive dislocation depinning from voids when the center of the voids is closer to the V-notch tip. When the distance between the V-notch tip and the voids is larger than $d = 30$ nm, we do not observe obvious effects of the presence of the complex V-notch tip stress field on the dislocation depinning angles ($d = 40$ nm in Fig. 5b and $d = 50$ nm in Fig. 5c).

We also investigated the effects of the different strain rates (10^7/s in Fig. 6a and 108/s in Fig. 6b, respectively) on the dislocation pinning–depinning from the voids with the spacing being $L \approx 155$ nm. From the two sets of simulations of the same specimen under the same tensile strain, it is found that the higher strain rate (Fig. 6b) leads to the stronger inertial effects and a larger dislocation depinning angle (Fig. 6b) from the void-2.

4. Summary and discussion

In summary, dynamic processes of dislocation bypass of voids with diameters of ~5 nm and spacing up to ~155 nm in Ni subjected to high strain rate loading have been simulated using the CAC method. Such large length scales are accessible only to massive MD simulations. Critical depinning cusp angles and dislocation line configurations have been determined. Atomic

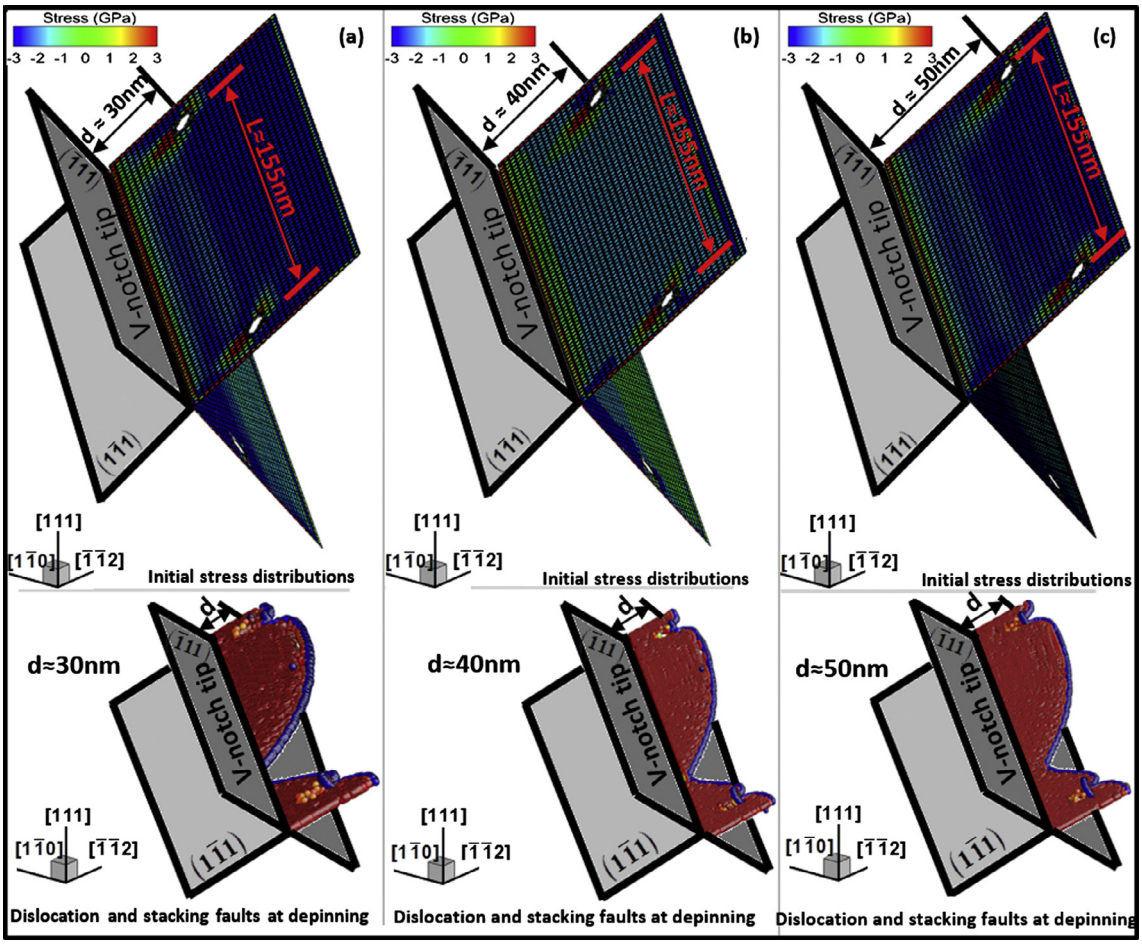

Fig. 5. Initial stress (σ_{23}) distributions, dislocation and stacking fault structures with the onset of the dislocation depinning from voids in Ni ($L \approx 155$ nm) under tension by CAC simulations: (a) $d \approx 30$ nm; (b) d≈40 nm; (c) $d \approx 50$ nm.

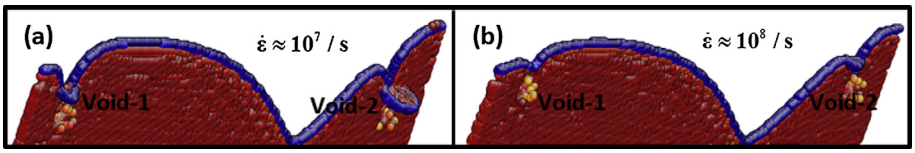

Fig. 6. Dislocation and stacking fault structures with the onset of the dislocation depinning from voids in Ni ($L \approx 155$ nm) for the same tensile strain at rates of: (a) $\dot{\varepsilon} \approx 10^7$/s; (b) $\dot{\varepsilon} \approx 10^8$/s.

scale mechanisms are identified, including drawing out of screw dipoles and nucleation and formation of Hirsch loops. This work has revealed a transition of a dislocation bypass/depinning mechanism induced by inertial effects under nonequilibrium high strain rate loading the obstacle spacing increases from several nm to hundreds of nm. Several sets of CAC simulations of dislocation pinning–depinning from the voids also show that: (1) closer proximity of voids to the notch tip increases inertial effects and leads to larger dislocation depinning angles; (2) higher strain rate also increases inertial effects.

In previous MD simulations, it has been found that atomic-scale details of dislocation–void interactions depend strongly on dislocation core structures. They also have demonstrated that the simple continuum line tension model widely used in estimations of critical resolved shear stress (CRSS) provides an incorrect relationship between applied stress and line shape. In addition, their dynamic simulations demonstrate that a dislocation moving at a high velocity can cut and breakaway from a void obstacle at stress significantly lower than the CRSS predicted by static line tension models. Results by Osetsky and Bacon show that the atomistic models can be employed to successfully investigate the characteristic mechanisms at the atomic level for dislocation–void interactions under both static ($T = 0$ K) and dynamic ($T > 0$ K) conditions. However, due to the inherent length scale limitations in full MD simulation, the largest voids spacing in their MD models is $L = 80$ nm.

As a consequence, the kinetic effects associated with the waves traveling along the long dislocation lines during dislocation–obstacle interactions cannot be fully captured although such kinetic effects seem to be very important for dynamic dislocation depinning from voids (Biztek and Gumbsch, 2005). In the present CAC models, the number of degree of freedom has been significantly reduced in the far field and thus the void spacing can be scaled up to $L = 155$ nm with the modest computational cost. With the void spacing scaled up to 155 nm, discovered a new physical mechanism through our CAC simulations: depinning of long dislocations from one void induces a wave traveling along the dislocation lines and this wave leads to larger depinning angles from the adjacent void with the same size.

Continuum line tension models have been used to describe the role of dislocation–void interactions (Coulomb, 1959; Scattergood and Bacon, 1982; Bitzek and Gumbsch, 2005). In static line tension models, the motion of dislocations and their interaction with void obstacles is described by assuming quasi-static migration of the dislocations. Initially, the strengthening effect of void obstacles was studied using the line tension approximation for isotropic solids (Coulomb, 1959). In the isotropic line tension model, according to the line tension approximation, the critical (maximum) stress, τ_c, is reached when the drawn-out screw dipole breaks free of a void. Scattergood and Bacon (1982) later developed an anisotropic continuum model for dislocation void interaction taking into account the non-local dislocation self-interaction, which was missing in the isotropic line tension approximation. In anisotropic line tension models, the dependence of τ_c on void diameter, D, and center-to-center spacing, $L + D$, for a periodic row of voids in a crystal at 0 K fits the relation

$$\tau_C = \frac{Gb}{2\pi L}\left[\ln\left(D^{-1} + L^{-1}\right)^{-1} + 1.52\right] \tag{4.1}$$

The dislocation depinning angle is then predicted as

$$\tau_C \approx \frac{Gb}{L}\cos\phi_c \tag{4.2}$$

In Eqs. (4.1) and (4.2), $G = 76$ GPa is the shear modulus, $b = 0.25$ nm is the magnitude of the Burgers vector of Ni, L is the void spacing and D is the void diameter. When $L = 155$ nm and $D = 5$ nm, according to the static line tension model, the dislocation depinning angle is predicted as $\phi_c = 0°$. Compared with our predictions in this work, $\phi_c \approx 70°$ (Fig. 4h), the depinning angles are underestimated in the static anisotropic line tension models because the inertial effects associated with dislocation motions have been completely ignored. Motivated by the possibility for dislocations to dynamically pass obstacles at lower stresses than required in a quasi-static process, Biztek and Gumbsch (2005) developed a dynamic line tension model (Biztek and Gumbsch, 2005) in which the inertial effects associated with dislocation dynamics have been included. The inertial effect is caused by the kinetic energy the dislocation has acquired during glide between obstacles, which allows the dislocation to overshoot its equilibrium position. In order to estimate the magnitude of inertial effects on dislocation passing void obstacles, in the dynamic line tension model by Biztek and Gumbsch (2005), the equation of motion of dislocation segments is solved numerically for a long dislocation, i.e.,

$$\frac{\partial}{\partial t}\left(m\frac{\partial x}{\partial t}\right) + B\frac{\partial x}{\partial t} - \Gamma\frac{\partial^2 y}{\partial x^2} = F \tag{4.3}$$

where F is the total accelerating force on the dislocation, m is the effective mass which determines the rate of acceleration, B is the damping coefficient which characterizes the deceleration by viscous drag, $B = 0.7$ μPa s in this work according to our recent measurement (Xiong et al., 2014b); Γ is the dislocation line tension. For a dislocation of length L with the boundary conditions $x(0,t) = x(L,t) = 0$ and initial conditions $x(y, t = 0) = 0; \dot{x}(y, t = 0) = 0$, when $B = 0.7$ μPa s and $L = 155$ nm, according to the dynamic line tension model, the dislocation will pass the obstacles at $\tau_{dyn} = 0.3\tau_C$, where τ_C is the static depinning stress. Then, according to $\tau_{dyn} \approx \frac{Gb}{L}\cos\phi_c^{dyn}$, the dislocation depinning angle can be predicted as $\phi_c^{dyn} \approx 70.6°$. Compared with our CAC simulation results $\phi_c \approx 70°$ in Fig. 4h, the dynamic line tension model does provide quite accurate guidance to investigate dislocation–void interactions in the presence of inertia effects. The dynamic line tension model can be used to estimate the magnitude of the inertial effects in the interaction of long dislocation lines with localized obstacles provided that Γ, m, B and the static obstacle strength τ_C are known. However, the direct observation of atomic-scale processes in dislocation–obstacle interaction is not possible in such dynamic line tension models. Therefore, for the interactions between the voids and long dislocation lines, although both the simple static and dynamic line tension models can provide approximate descriptions, such continuum line tension models are not predictive since the atomistic nature of dislocations have been smeared out. The present CAC method provides an alternative approach in predicting dynamic strength of the void obstacles for the long dislocation lines, including atomistic details such as dislocation disassociation and formation of Hirsch loops around the voids, while capturing dislocation dynamics in the far field.

Although this work is motivated by the need to obtain better understanding of irradiation hardening at elevated temperatures, here we only investigate the dislocation pinning–depinning mechanisms at low temperatures, ignoring thermomechanical coupling effects on dislocation pinning–depinning processes. At elevated temperature, thermomechanical coupling becomes important and thus the energy equations together with the balance equation of linear momentum in the atomistic field theory (Chen, 2009) need to be solved.

Acknowledgements

The authors are grateful for the support of a collaborative National Science Foundation research grant (McDowell, CMMI-1232878 and Chen, CMMI-1233113) to further advance and apply the CAC method, which in its present form is a culmination of developments supported in part by NSF – United States (CMMI 1129976), DARPA – United States (N66001-10-1-4018), and Department of Energy – United States (DOE/DE-SC0006539) (Chen and Xiong). Any opinions, findings, and conclusions or recommendations expressed in this material are those of the authors and do not necessarily reflect the views of the National Science Foundation, DARPA or DOE. This research was also supported in part by the National Science Foundation through Teragrid resources provided by TACC.

References

Amodeo, R.J., Ghoniem, N.M., 1990a. Dislocation dynamics. I. A proposed methodology for deformation micromechanics. Phys. Rev. B 41, 6958–6967.
Amodeo, R.J., Ghoniem, N.M., 1990b. Dislocation dynamics. II. Applications to the formation of persistent slip bands, planar arrays, and dislocation cell. Phys. Rev. B 41, 6968–6976.
Averback, R.S., Benedek, R., Merkle, K.L., 1977. Defect production in copper and silver by light energetic ions. Appl. Phys. Lett. 30, 455.
Bacon, D.J., Osetsky, Y.N., 2005. Modelling dislocation obstacle interactions in metals exposed to an irradiation environment. Mater. Sci. Eng. A. 400–401, 353.
Bacon, D.J., Osetsky, Y.N., Rong, Z., 2006. Computer simulation of reactions between an edge dislocation and glissile self-interstitial clusters in iron. Philos. Mag. 86, 3291.
Bacon, D., Osetsky, Y., Rodney, D., 2009. Dislocation–obstacle interactions at the atomic level. In: Hirth, J., Kubin, L. (Eds.), Dislocations in Solids, vol. 15, pp. 1–90 (chapter 88).
Bitzek, E., Gumbsch, P., 2004. Atomistic study of drag, surface and inertial effects on edge dislocations in face centered cubic metals. Mater. Sci. Eng. A 287–289, 11–15.
Bitzek, E., Gumbsch, P., 2005. Dynamic aspects of dislocation motion: atomistic simulations. Mater. Sci. Eng. A 400–401, 40–44.
Brown, L.M., Stobbs, W.M., 1971. The work-hardening of copper-silica. I. A model based on internal stresses, with no plastic relaxation. Philos. Mag. 23, 1201.
Bulatov, V.V., Abraham, F.F., Kubin, L., Devincre, B., Yip, S., 1998. Connecting atomistic and mesoscale simulations of crystal plasticity. Nature 391, 669–672.
Cai, W., Bulatov, V.V., 2004. Mobility laws in dislocation dynamics simulations. Mater. Sci. Eng. A 387, 277.
Chen, Y., 2006. Local stress and heat flux in atomistic systems involving three-body forces. J. Chem. Phys. 24, 054113.
Chen, Y., 2009. Reformulation of microscopic balance equations for multiscale materials modeling. J. Chem. Phys. 130, 134706.
Chen, Y., Lee, J.D., 2005. Atomistic formulation of a multiscale field theory for nano/micro solids. Philos. Mag. 85, 4095–4126.
Chen, Y., Zimmerman, J., Krivtsov, A., McDowell, D.L., 2011. Assessment of atomistic coarse-graining methods. Int. J. Eng. Sci. 49, 1337–1349.
Cheng, Y., Bitzek, E., Weygand, D., Gumbsch, P., 2010. Atomistic simulation of dislocation–void interactions under cyclic loading. Modell. Simul. Mater. Sci. Eng. 18, 025006.
Coulomb, P., 1959. Sur le blocage des dislocations par des cavites ou de petits precipites. Acta Metall. 7, 556.
Crocombette, J.P., Proville, L., 2011. Thermal conductivity degradation induced by point defects in irradiated silicon carbide. Appl. Phys. Lett. 98, 191905.
David, M.L., Pailloux, F., Mauchamp, V., Pizzagalli, L., 2011. In-situ probing of helium desorption from individual nanobubbles under electron irradiation. Appl. Phys. Lett. 98, 171903.
Daw, M.S., Baskes, M.I., 1984. Embedded-atom method: derivation and application to impurities, surfaces, and other defects in metals. Phys. Rev. B 29, 6443–6453.
Demkowicz, M.J., Bhattacharyya, D., Usov, I., Wang, Y., Nastasi, M., Misra, A., 2010. The effect of excess atomic volume on He bubble formation at fcc-bcc interfaces. Appl. Phys. Lett. 97, 161903.
Donnelly, S.E., Lucas, A.A., Rife, J.C., 1983. Vacuum ultraviolet fluorescence of helium in bubbles in aluminum and tin. Appl. Phys. Lett. 43, 35.
Fago, M., Hayes, R.L., Carter, E.A., Ortiz, M., 2004. Density-functional-theory-based local quasicontinuum method: prediction of dislocation nucleation. Phys. Rev. B 70, 100102(R).
Fusenig, K.D., Nembach, E.E., 1993. Dynamic dislocation effects in precipitation hardened materials. Acta Metall. Mater. 41, 3181–3189.
Granato, A.V., 1971. Dislocation inertial effects in the plasticity of superconductors. Phys. Rev. B 4, 2196–2201.
Harry, T., Bacon, D.J., 2002. Computer simulation of the core structure of the ⟨1 1 1⟩ screw dislocation in α-iron containing copper precipitations-I. Structure in the matrix and a precipitate. Acta Mater. 50, 195.
Hatano, T., 2006. Dynamics of a dislocation bypassing an impenetrable precipitate: the Hirsch mechanism revisited. Phys. Rev. B 74, 020102.
Henriksson, K.O.E., Nordlund, K., Krasheninnikov, A., Keinonen, J., 2005. Difference in formation of hydrogen and helium clusters in tungsten. Apply. Phys. Lett. 87, 163113.
Hirsch, P.B., Silcox, J., Smallman, R.E., Westmacott, K.H., 1958. Dislocation loops in quenched aluminium. Philos. Mag. 3 (32), 897.
Hirth, J.P., Lothe, J., 1982. Theory of Dislocations. John Wiley & Sons, New York.
Hu, S.Y., Baskes, M.I., Stan, M., 2007. Phase-field modeling of microvoid evolution under elastic–plastic deformation. Appl. Phys. Lett. 90, 081921.
Hull, D., Bacon, D.J., 2001. Introduction to Dislocations, fourth ed. Butterworth-Heinemann.
Irving, J., Kirkwood, J., 1950. The statistical mechanical theory of transport processes. IV. The equations of hydrodynamics. J. Chem. Phys. 8, 817.
Kiritani, M., Satoh, Y., Kizuka, Y., Arakawa, K., Ogasawara, Y., Arai, S., et al, 1999. Anomalous production of vacancy clusters and the possibility of plastic deformation of crystalline metals without dislocations. Philos. Mag. Lett. 79, 797.
Kirkwood, J., 1946. The statistical mechanical theory of transport processes. I. General theory. J. Chem. Phys. 1946 (14), 180–201.
Kluth, S.M., Gerald, J.D.F., Ridgway, M.C., 2005. Ion-irradiation-induced porosity in GaSb. Appl. Phys. Lett. 86, 131920.
Kondo, S., Katoh, Y., Snead, L., 2008. Unidirectional formation of tetrahedral voids in irradiated silicon carbide. Appl. Phys. Lett. 93, 163110.
Kubin, L.P., Canova, G., 1992. The modelling of dislocation patterns. Scr. Metall. Mater. 27 (8), 957–962.
Kulkarni, Y., Knap, J., Ortiz, M., 2008. A variational approach to coarse graining of equilibrium and non-equilibrium atomistic descriptions at finite temperature. J. Mech. Phys. Solids 56, 1417–1449.
Li, J., 2003. AtomEye: an efficient atomistic configuration viewer. Modell. Simul. Mater. Sci. Eng. 11, 173.
McDowell, D.L., 2010. A perspective on trends in multiscale plasticity. Int. J. Plast. 26, 1280–1309.
Mishin, Y., Farkas, D., Mehl, M.J., Papaconstantopoulos, D.A., 1999. Interatomic potentials for monoatomic metals from experimental data and ab initio calculations. Phys. Rev. B 59, 3393.
Mishin, Y., Mehl, M.J., Papaconstantopoulos, D.A., Voter, A.F., Kress, J.D., 2001. Structural stability and lattice defects in copper: Ab initil, tight-binding and embedded-atom calculations. Phys. Rev. B 63, 224106.
Osetsky, Y.N., Bacon, D.J., 2003. Void and precipitate strengthening in alpha-iron: what can we learn from atomic level modeling. J. Nucl. Mater. 323, 268.
Scattergood, R.O., Bacon, D.J., 1982. The strengthening effect of voids. Acta Metall. 30, 1665.
Shehadeh, M.A., Bringa, E.M., Zbib, H.M., McNaney, J.M., Remington, B.A., 2006. Simulation of shock-induced plasticity including homogeneous and heterogeneous dislocation nucleations. Appl. Phys. Lett. 89, 171918.

Shilkrot, L.E., Curtin, W.A., Miller, R.E., 2002a. A coupled atomistic/continuum model of defects in solids. J. Mech. Phys. Solids 2002 (50), 2085–2106.
Shilkrot, L.E., Miller, R.E., Curtin, W.A., 2002b. Coupled atomistic and discrete dislocation plasticity. Phys. Rev. Lett. 89, 025501–025504.
Shilo, D., Zolotoabko, E., 2003. Stroboscopic X-ray imaging of vibrating dislocations excited by 0.58 GHz phonons. Phys. Rev. Lett. 91, 115506.
Shilo, D., Zolotoabko, E., 2007. X-ray imaging of phonon interaction with dislocations. Dislocations in Solids, vol. 13. Elsevier, Amsterdam (chapter 80).
Shim, J.H., Cho, Y.W., Kwon, S.C., Kim, W.W., Wirth, B.D., 2007. Screw dislocation assisted martensitic transformation of a bcc Cu precipitate in bcc Fe. Appl. Phys. Lett. 90, 021906.
Shingo, K., Miura, K., Fujita, K., Hirao, K., Si, J., Shibata, N., et al, 2007. Optically produced cross patterning based on local dislocations inside MgO single crystals. Appl. Phys. Lett. 90, 163110.
Tadmor, E.B., Ortiz, M., Phillips, R., 1996. Quasicontinuum analysis of defects in solids. Philos. Mag. A 73, 1529–1563.
Terentyev, D., Malerba, L., Bacon, D.J., Osetsky, Y.N., 2007. The effect of temperature and strain rate on the interaction between an edge dislocation and an interstitial dislocation loop in alpha-iron. J. Phys.: Condens. Matter 19, 456211.
Van der Giessen, E., Needleman, A., 1995. Discrete dislocation plasticity: a simple planar model. Model. Simul. Mater. Sci. Eng. 3, 689–735.
Weiner, J.H., Hikata, A., Elbaum, C., 1976. Vibration of a pinned dislocation segment in an atomistic model. Phys. Rev. B. 13, 531–543.
Wu, X.L., Li, B., Ma, E., 2007. Vacancy clusters in ultrafine grained Al by severe plastic deformation. Appl. Phys. Lett. 91, 141908.
Wusatowska-Sarnek, A.M., Miura, H., Sakai, T., 1999. Coherency strains influence on martensitic transformation of γ-Fe particles in compressed Cu–Fe alloy single crystals. J. Mater. Sci. 34, 5477.
Xiong, L., Tucker, G., McDowell, D.L., Chen, Y., 2011. Coarse-grained atomistic simulation of dislocations. J. Mech. Phys. Solids 59, 160–177.
Xiong, L., Deng, Q., Tucker, G., McDowell, D.L., Chen, Y., 2012a. A concurrent scheme for passing dislocations from atomistic to continuum domains. Acta Mater. 60, 899–913.
Xiong, L., Deng, Q., Tucker, G., McDowell, D.L., Chen, Y., 2012b. Coarse-grained atomistic simulations of dislocations in Al, Ni and Cu crystals. Int. J. Plast. 38, 86–101.
Xiong, L., McDowell, D.L., Chen, Y., 2014a. Sub-THz phonon drag on dislocations by coarse-grained atomistic simulations. Int. J. Plast. 55, 268–278.
Xiong, L., Chen, X., Zhang, N., McDowell, D.L., Chen, Y., 2014b. Prediction of phonon properties of 1D polyatomic systems using concurrent atomistic–continuum simulation. Arch. Appl. Mech., 1–11.
Zamora, R.J., Nair, A.K., Hennig, R.G., Warner, D.H., 2012. Ab initio prediction of environmental embrittlement at a crack tip in aluminum. Phys. Rev. B 86, 060101 (R).
Zbib, H.M., Rhee, M., Hirth, J.P., 1998. On plastic deformation and the dynamics of 3D dislocations. Int. J. Mech. Sci. 40, 113–127.
Zhou, M., McDowell, D.L., 2002. Equivalent continuum for dynamically deforming atomistic particle systems. Philos. Mag. A 82 (13), 2547–2574.
Zhou, S.J., Preston, D.L., Lomdahl, P.S., Beazley, D.M., 1998. Large-scale molecular dynamics simulations of dislocation intersection in copper. Science 279 (5356), 1525–1527.
Zinkle, S.J., 2005. Fusion materials science: overview of challenges and recent progress. Phys. Plasmas 12, 058101.